Spin-Orbit-Torque Efficiency and Current-Driven Coherent Magnetic Dynamics in a Pt/Ni/Py Trilayer-Based Spin Hall Nano-Oscillator

Lina Chen,[1,2] Xiang Zhan,[2] Kaiyuan Zhou,[2] Wenqiang Wang,[2] Like Liang◉,[2] Zhenyu Gao◉,[2]
Y.W. Du,[2] and R.H. Liu◉[2,*]

[1]*School of Science, Nanjing University of Posts and Telecommunications, Nanjing 210023, China*

[2]*Jiangsu Provincial Key Laboratory for Nanotechnology, National Laboratory of Solid State Microstructures and School of Physics, Nanjing University, Nanjing 210093, China*

We experimentally study the current-induced effective spin-orbit torque (SOT) efficiency and the spectral characteristics of current-driven coherent magnetic dynamics in spin Hall nano-oscillators (SHNOs) based on the Pt/Ni/Py trilayer. We determine that the Pt/Ni/Py trilayer structure has an effective damping-like torque efficiency $\xi_{DL} \sim 0.055$, comparable with the Pt/Co and Pt/Fe bilayer systems with a strong interfacial spin-orbit coupling and magnetic proximity effect. Furthermore, the microwave-generation spectra show that the Pt/Ni/Py-based SHNOs exhibit a single nonlinear self-localized bullet mode with a frequency below f_{FMR} and a significant current-dependent frequency red shift due to its strong nonlinear effect, which is very similar to that in Pt/Py-based SHNOs, at low oblique angles $\varphi \leq 50°$. In contrast, at high oblique angles $\varphi \geq 55°$, the spectra show two oscillating peaks with very similar field-, current-, and temperature-dependent behaviors, which suggests the spatial coexistence of two same-type nonlinear self-localized bullet modes at certain currents and magnetic fields. Additionally, the observed linear temperature dependence of the minimum line width, which resembles the thermal broadening of single-mode oscillation, further confirms that two localized bullet modes are independent, spatially separated, and lack thermally activated mode-transition behavior. Our results provide valuable information for the electronic control of coherent magnetic dynamics by combining bulk and interfacial spin-orbit coupling effects in the magnetic heterostructures.

I. INTRODUCTION

The electrical manipulation of controllable magnetization reversal [1–4] and coherent precession [5,6] through current-induced spin-orbit torques in heavy-metal–ferromagnet (HM/FM) bilayer systems provides a promising path to develop high energy efficiency, high-speed nonvolatile magnetic memory, rf electronics, spin-wave-based electronic devices, and neuromorphic computing [7–12]. The spin-orbit torques are related to bulk spin-orbit coupling (SOC) in the HM [13–15] and interfacial SOC at the HM-FM interface [16,17]. The bulk SOC of the HM causes the spin-dependent scattering and generates a pure spin current perpendicular to the transversal charge current and vertically injected into the adjacent FM, called the spin Hall effect (SHE) [13–15]. However, the spin current generated by the bulk SHE of the HM can drop significantly at the HM-FM interface due to the degradation of the interfacial spin transparency by spin back flow and spin memory loss (SML), which are

highly dependent on materials-dependent interface parameters [18–20]. The interfacial SOC in the HM/FM bilayer also generates a spin accumulation at the interface with broken inversion symmetry due to the interfacial Rashba effect [16,17,21–23]. In addition, recent reports have found a considerable spin Hall angle in the weakly spin-orbit coupled 3d light metals and FM bilayer systems [24–26].

The current-induced spin current can excite coherent magnetization precession of a nanomagnet that is called a spin-current nano-oscillator or a spin Hall nano-oscillator (SHNO) [5,6,27]. Many SHNOs with various device geometries (e.g., triangular nanogap contacts and vertical contact on extended magnetic films, nanowires, and single and multiple nanoconstrictions) and several HM and FM materials—Pt, W, Ta, permalloy (Py), [Co/Ni]$_n$, Co-Fe-B, and yttrium iron garnet (YIG)—based on HM/FM bilayers have been studied [5,6,11,28–35]. Previous studies show that the coherent spin dynamics in SHNOs, excited by the current-induced spin-orbit torque, are highly related to the spatial distribution of spin-current injection and the bulk and interface magnetic properties of FM materials. For example, a primary self-localized nonlinear bullet

---

*rhliu@nju.edu.cn

spin-wave mode, a secondary side mode, the coexistence of multiple modes, and mutual synchronization behavior are observed in SHNOs with extended in-plane magnetization Py film [6,36,37], while in SHNOs with out-of-plane magnetization due to strong interfacial perpendicular magnetic anisotropy or a large oblique external magnetic field, in addition to the self-localized bullet mode, linear propagating [31,35,38,39], localized magnetic bubble skyrmion [31,38], and magnetic droplet modes [40,41] have also been demonstrated by experiments and micromagnetic simulations.

Therefore, additional experimental studies on the relationship between the magnetization dynamics of SHNOs and various FM materials or interfacial parameters can help us to understand better how the bulk SOC in the HM and the interfacial SOC at HM-FM and FM1-FM2 interfaces affect the SOT efficiency and the SOT-induced nonlinear spin-wave behavior in the HM/FM1/FM2 trilayer with broken inversion symmetry. Unlike the Pt-Co and Pt-Fe interfaces with a strong interfacial SOC and magnetic proximity effect, which exhibits a large interfacial Rashba SOT due to the current-induced spin accumulation, large interface magnetic anisotropy, strong spin back flow, and large SML at their interfaces [19,20,23], the Pt-Ni interface has a much smaller magnetic proximity effect and interfacial SOC. In consequence, it is expected that the Pt/Ni bilayer exhibits a comparable small spin back flow and SML and a small Rashba SOT at the interface [42,43]. However, the Ni thin film has a much lower Curie temperature T_c and smaller saturation magnetization M_s than Co, Fe, and Py thin films.

To improve the T_c and M_s of the free FM layer in the studied SHNOs, we adopt the Ni/Py bilayer as the ferromagnetic layer to experimentally study the current-induced effective SOT efficiency by using spin-torque ferromagnetic resonance (ST FMR) and the exciting current, magnitude, and angle of the applied magnetic field and the temperature dependencies of the microwave-generation spectral characteristics. In contrast to Pt/[Co/Ni]-based SHNOs with three spin-wave modes, including the nonlinear self-localized bullet, linearly propagating, and localized magnetic bubble skyrmion or droplet modes, Pt/Ni/Py-based SHNOs only excite a nonlinear self-localized bullet mode with a frequency below f_{FMR}, under the in-plane and low oblique angles $\varphi \leq 50°$ magnetic field experimental geometry. However, under high oblique angles $\varphi \geq 55°$, there is a region where two nonlinear self-localized bullet modes of the same type with distinct frequencies coexist under certain currents and magnetic fields. In addition, the minimum line width exhibits a linear temperature dependence, in contrast to the exponential temperature dependence observed in Pt/Py. These distinct different dynamic characteristics of the Pt/Py system are closely related to the significant difference in interface-induced magnetic anisotropy between Pt-Ni and Pt-Py interfaces
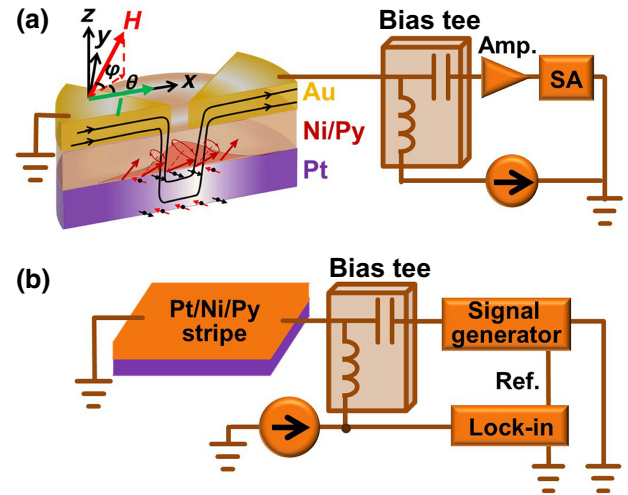

FIG. 1. (a) A schematic of the SHNO device structure and the experimental setup of the microwave-generation characteristics of a nanogap SHNO with the orientation of the applied magnetic field H, where φ is defined as the out-of-plane tilt angle of H and θ is the angle between the directions of the current I and the in-plane component of the magnetic field H: SA, spectrum analyzer. (b) A schematic of the ST-FMR measurement setup.

and the magnetostriction coefficient between Ni and Py layers.

II. EXPERIMENTAL

The films of Pt(4 nm)/Ni(2.5 nm)/Py(1.5 nm) are deposited by dc magnetron sputtering on annealed sapphire substrates with (0001) orientation. The base pressure before the deposition is less than 2×10^{-8} Torr and the Ar pressure during deposition is $\simeq 3.7$ mTorr. The films are also covered *in situ* by a 2–3 nm SiO_2 capping layer to prevent the top Py from oxidizing when exposed to the atmosphere. Similar to the previously reported nanogap spin Hall auto-oscillators [5,31], our SHNO device is based on a Pt/Ni/Py trilayer disk with a diameter of 4 μm. The top two Au(100 nm) triangle electrodes with an approximately 70-nm gap are deposited on the Pt/Ni/Py trilayer disk to achieve the highly localized current density in the Pt layer within the gap area [Fig. 1(a)]. The device is fabricated by a combination of magnetron sputtering and electron-beam lithography.

The effective SOT efficiency and the uniform FMR dynamic behavior of the Pt/Ni/Py trilayers are determined first by the widely used standard ST-FMR technique [44]. Figure 1(b) shows the ST-FMR experimental layout, where the Pt/Ni/Py trilayer is patterned into a 5 × 10 μm^2 rectangular shape, similar to the previous studies [45]. In the ST-FMR experiment, a rf current I_{rf} passes through the trilayer stripe along its longitudinal direction, causing magnetization oscillation driven by a combination of an rf-current-induced Oersted field and SOTs due to SOC.

The oscillating magnetization causes periodic variation of resistance due to anisotropic magnetoresistance (AMR) [46] and, mixed with the I_{rf}, produces a dc voltage V_{dc} due to the rectification effect. The efficiency of spin torque on the magnetization **M** in SOT-based devices is proportional to the component of **M** perpendicular to the current direction I (or parallel to the polarization direction of the spin current). Meanwhile, the AMR of the magnetic layer has a sinusoidal dependence on the in-plane angle θ between **M** and I. In other words, the maximal efficiency of ST in both ST-FMR and SHNO devices corresponds to the minimum of the AMR where the in-plane magnetic field H is orthogonal to I. Therefore, we carry out all the ST-FMR and auto-oscillation spectra measurements described below at the geometry of the in-plane component of the applied magnetic field forming an angle $\theta = 60°$ with respect to the current direction by trading off a reduction in the efficiency of ST for a sizable generation microwave signal due to the AMR effect.

III. RESULTS AND DISCUSSION

A. ST-FMR spectra and its current modulation with an in-plane field

The ST-FMR spectra of Pt(4 nm)/Ni(2.5 nm)/Py(1.5 nm) are recorded by scanning the in-plane magnetic field with different excitation frequencies from 5 to 16 GHz. Figure 2(a) shows that the obtained ST-FMR signal V_{dc} can be fitted well by the sum of a symmetric and an antisymmetric Lorentzian function as follows:

$$V_{dc} = V_S \frac{\Delta H^2}{(H - H_{res})^2 + \Delta H^2} + V_A \frac{\Delta H(H - H_{res})}{(H - H_{res})^2 + \Delta H^2},$$
(1)

where the fitting parameters V_S, V_A, ΔH, and H_{res} are the magnitude of the symmetric component, the antisymmetric component, the line width, and the resonance field, respectively. Figures 2(b) and 2(c) show the extracted resonance field H_{res} versus f and the line width ΔH versus f data, which can be used to estimate the effective demagnetizing field $4\pi M_{eff} = 5.0$ kOe based on the FMR Kittel formula $f = \gamma\sqrt{H(H + 4\pi M_{eff})}$ and the damping constant $\alpha = 0.047$, given by a linear fitting of frequency-dependent line width using $\Delta H = \Delta H_0 + \alpha f/\gamma$, where $\gamma = 2.8$ GHz/kOe is the gyromagnetic ratio. We note that the interfacial effect of Pt/Ni and Ni/Py could result in uniaxial magnetic anisotropy with the anisotropy axis normal to the film. This contribution can be taken into account as an additional term in the effective demagnetizing field $4\pi M_{eff} = 4\pi M_s - (2K_u/M_s t_F)$, where M_s is the saturation magnetization, K_u is the anisotropy coefficient of the multilayer, and t_F is the thickness of the Ni/Py layer. The interfacial perpendicular magnetic anisotropy coefficient K_u is 0.26 erg/cm^2, using the saturation magnetization
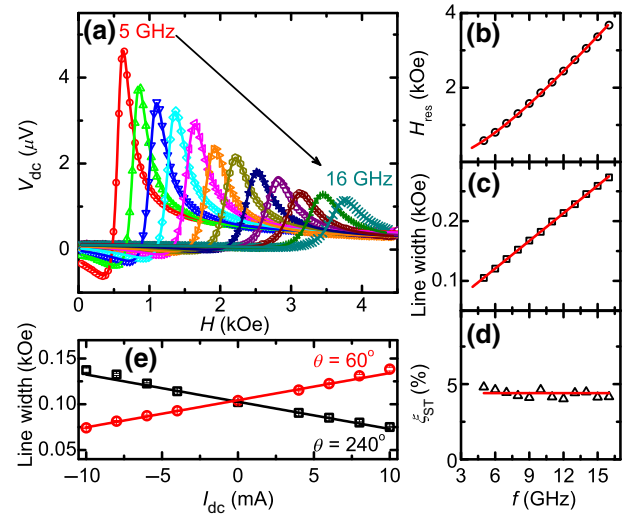

FIG. 2. The ST-FMR spectra of the Pt(4 nm)/Ni(2.5 nm)/Py(1.5 nm) trilayer with an in-plane magnetic field. (a) The symbols show the ST-FMR voltage V_{dc} versus the in-plane magnetic field H obtained with various excitation frequencies from 5 to 16 GHz with a 1-GHz step at an angle $\theta = 60°$ between the in-plane field H and the direction of the current I and at room temperature. The curve is the best fit with a sum of a symmetric and an antisymmetric Lorentzian function [see Eq. (1)]. (b)–(d) The dependence of (b) the resonance field H_{res}, (c) the line width ΔH, and (d) the effective spin-torque efficiency ξ_{DL} on the excitation frequency f. The solid curve in (b) is the fitting result of the FMR data using the Kittel formula. The solid line in (c) is the best fit of the frequency-dependent line width ΔH data using $\Delta H = \Delta H_0 + \alpha f/\gamma$, with $\Delta H_0 = 28$ Oe and $\alpha = 0.047$. The solid line in (d) is the average value of $\xi_{FMR} = 0.045$, determined from Eq. (2). (e) The dependence of the line width ΔH on I_{dc} with $f = 5$ GHz at $\theta = 60°$ and $240°$, respectively. The solid lines are the linear fits.

$M_s = 580$ emu/cm^3 of thin film independently measured by a vibration sample magnetometer (VSM). The damping constant $\alpha = 0.047$ is significantly higher than the 0.028 observed in Pt(5 nm)/Py(4 nm) [44], which is related to the additional magnon scattering at Pt-Ni and Ni-Py interfaces due to the interfacial SOC and the larger magnetoelastic efficiency in Ni, except for the expected spin-pumping effect in Pt/Ni due to spin-current generation.

Furthermore, adopting the method commonly used in such bilayer systems, we can quantitatively estimate the FMR spin-torque generation efficiency ξ_{FMR} of this Pt/Ni/Py trilayer structure by line-shape analysis of the ST-FMR spectra as follows [44]:

$$\xi_{FMR} = \frac{V_S}{V_A} \frac{e\mu_0 M_s t_N t_F}{\hbar}[1 + (4\pi M_{eff}/H_{res})]^{1/2}, \quad (2)$$

where e is the elementary charge, μ_0 is the magnetic permeability of vacuum, and M_s, t_N, t_F, V_S, and V_A are the saturation magnetization of the Ni/Py bilayers, the thickness

of Pt and the ferromagnetic Ni/Py bilayers, and the symmetric and antisymmetric components of V_{dc}, respectively. The symmetric voltage signal V_S is caused by the damping-like out-of-plane effective field H_{DL}, while V_A comes from the in-plane effective field, which is the sum of the current-induced Oersted field H_{Oe} caused by the current flow in the Pt layer and the effective fieldlike field H_{FL}. Figure 2(d) shows the calculated ξ_{FMR} under the different excitation frequencies, and its average value is 0.045, lower than the previously reported 0.056 ± 0.005 in Pt(6 nm)/Py(4 nm) [44]. The difference suggests that the Pt-Ni interface has spin transmission due to spin back flow and SML, and interfacial fieldlike torque efficiency and/or its sign different from the Pt/Py system [19,20,42,43] because ξ_{FMR} includes both dampinglike and fieldlike torque efficiencies. Note that these two spin-torque efficiencies can be separated by analyzing the ST-FMR spectra for the devices by varying the FM-layer thickness t_F using $1/\xi_{FMR} = 1/\xi_{DL}(1 + \hbar\xi_{FL}/e\mu_0 M_s t_N t_F)$ [18,43].

However, we adopt an alternative method to estimate the effective dampinglike torque efficiency ξ_{DL} by analyzing the modulation of the ST-FMR line width by dc. Figure 2(e) shows the current-dependent line width ΔH at two angles, $\theta = 60°$ and $240°$. $\xi_{DL} = 0.055$ can be determined through fitting current-dependent line-width ΔH data [Fig. 2(e)] using the following formula [44,47,48]:

$$\xi_{DL} = \frac{\delta\Delta H/\delta I}{\frac{\hbar f}{2e\gamma}\frac{\sin\theta}{(H_{res}+2\pi M_{eff})\mu_0 M_s t_F}}\frac{R_{Ni/Py}+R_{Pt}}{R_{Ni/Py}}A_C, \quad (3)$$

where $\hbar$ is the Dirac constant, R_{Pt} and $R_{Ni/Py}$ are the resistance of the HM Pt and the ferromagnetic Ni/Py bilayer, respectively, and A_C is the short cross-section area of the ST-FMR device. The Pt/Ni/Py trilayer has $\xi_{DL} = 0.055$, higher than the $\xi_{FMR} \simeq 0.045$ obtained by analyzing the line shape of the ST-FMR spectra above; this indicates that the Pt-Ni interface has a considerable fieldlike torque efficiency ξ_{FL} with the same sign as ξ_{DL}, consistent with the previously reported $\xi_{DL} \sim 0.05$ and a non-negligible ξ_{FL} in Pt/Ni bilayers by varying the Ni layer thickness [43].

B. ST-FMR spectra with varying out-of-plane angle

To directly compare the relation of the observed current-induced SOT driven spin-wave modes observed in Sec. III C to the spin-wave spectrum of the extended Ni/Py film, we also examine the out-of-plane angular-dependent ST-FMR spectra. Figure 3 shows the representative ST-FMR spectra obtained at a fixed excitation frequency $f = 5$ GHz, $\theta = 60°$, various polar angles φ, and room temperature. The ST-FMR spectra can be fitted well by the Lorentzian function given in Eq. (1) and the resonant field H_{res} and line width ΔH can be accurately extracted, as shown in Figs. 3(b) and 3(c), respectively. According to the previous studies on out-of-plane FMR spectra of thin
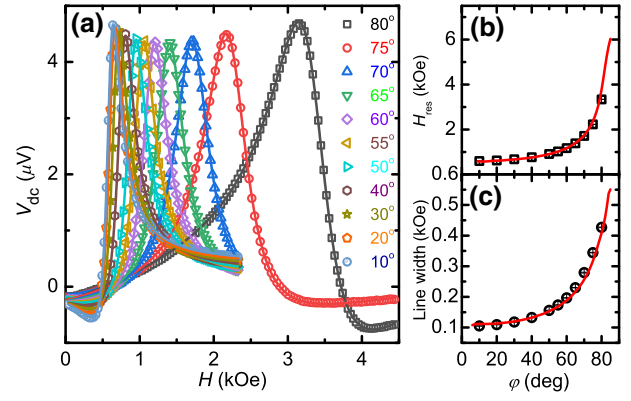

FIG. 3. The ST-FMR spectra of the Pt/Ni/Py trilayer with an out-of-plane magnetic field. (a) The symbols show the ST-FMR voltage V_{dc} versus the out-of-plane magnetic field H obtained at various labeled azimuth angles φ and an in-plane angle $\theta = 60°$, $f = 5$ GHz, and room temperature. The curve is the best fit with the sum of a symmetric and an antisymmetric Lorentzian function [see Eq. (1)]. (b), (c) The dependence of (b) the resonance field H_{res} and (c) the line width on the out-of-plane angle φ. The solid curves are the results of fitting the FMR data using Eq. (4) with the effective magnetization $4\pi M_{eff} = 4.9$ kOe and Eq. (5) with a damping constant $\alpha = 0.05$, respectively.

film [49,50], the polar angular-dependent resonance field H_{res} of the FMR spectra is determined by

$$\begin{cases} (\frac{f}{\gamma})^2 = [H_{res}\cos(\varphi_H - \varphi_M) - 4\pi M_{eff}\sin^2(\varphi_M)] \\ \qquad \times [H_{res}\cos(\varphi_H - \varphi_M) + 4\pi M_{eff}\cos(2\varphi_M)] \\ 4\pi M_{eff}\sin(2\varphi_M) = 2H_{res}\sin(\varphi_M - \varphi_H), \end{cases} \quad (4)$$

where φ_H and φ_M are the out-of-plane angles of the applied external magnetic field and the magnetization, respectively. The solid red line in Fig. 3(b) is the fitting result of the resonant field H_{res} as a function of the external field orientation φ_H at $f = 5$ GHz using Eq. (4). The obtained fitting parameter $4\pi M_{eff} = 4.9$ kOe is highly consistent with the value of 5.0 kOe determined by the f versus H_{res} dispersion curve with an in-plane orientation.

Meanwhile, the intrinsic damping constant α can also be extracted from the out-of-plane angular-dependent line-width data in Fig. 3(c). The angular-dependent line width due to intrinsic damping of the magnetization precession can be expressed as [49]

$$\Delta H = \Delta H_0 + \alpha[H_{res}\cos(\varphi_H - \varphi_M) \\ - 2\pi M_{eff}(3\sin^2(\varphi_M) - 1)]\left|\frac{d(f/\gamma)}{dH_{res}}\right|^{-1}, \quad (5)$$

where ΔH_0 is the line width due to the distribution of H_{res} related to magnetic inhomogeneities. The experimental ΔH_0 versus φ_H data are fitted well by Eq. (5) with a fitting
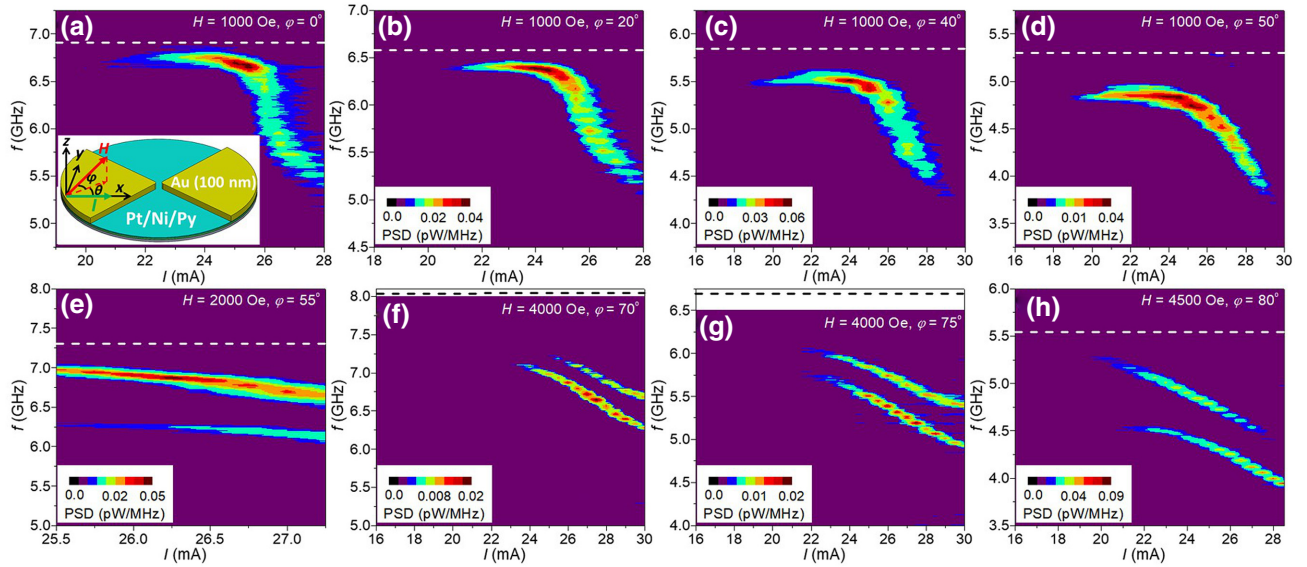
FIG. 4. The dependence of the microwave-generation characteristics of the Pt(4 nm)/Ni(2.5 nm)/Py(1.5 nm)-based nanogap SHNO on the current at 6 K with several different magnetic fields forming an out-of-plane tilting angle φ with respect to the film plane. (a)–(d) Pseudocolor maps of the power spectral density (PSD) of the generated microwave signal with a single peak, for varying currents I in 0.5-mA steps, at low magnetic field $H = 1000$ Oe and four low out-of-plane tilting angles (a) $\varphi = 0°$, (b) $20°$, (c) $40°$, and (d) $50°$. (e)–(h) Pseudocolor maps of the PSD with two main peaks obtained at high magnetic fields (e) $H = 2000$ Oe and the large out-of-plane tilting angle $\varphi = 55°$, (f) $H = 4000$ Oe and $\varphi = 70°$, (g) $H = 4000$ Oe and $\varphi = 75°$, and (h) $H = 4500$ Oe and $\varphi = 80°$. The dashed curves represent the corresponding FMR frequencies, f_{FMR}, of the Pt/Ni/Py trilayer, obtained using the ST-FMR technique. The inset in (a) is a schematic of the device structure and the experimental setup of the studied SHNO.

C. Current-driven coherent dynamical modes at $T = 6$ K

To experimentally explore the coherent magnetic dynamics of the Ni/Py bilayer excited by a combination of spin current generated by the SHE in the Pt layer and the spin accumulation at the Pt-Ni interface, we further carry out spectroscopic measurements on the nanogap-SHNO device with different magnetic fields H, orientations φ, and excitation currents I. The SHNO-device structure and experimental layout, shown in Fig. 1(a) and the inset of Fig. 4(a), are the same in as our previously reported spin Hall nano-oscillator based on a Py/Pt bilayer with a negligible in-plane magnetic anisotropy (IMA) [6] or a Pt/[Co/Ni] multilayer with a well-defined perpendicular magnetic anisotropy (PMA) [31].

Similar to the soft magnetic Py, the pure-Ni film also has a large AMR [46]. Meanwhile, the Ni has a low Curie temperature, a large magnetostrictive coefficient due to its bulk SOC and unique electronic structure, and considerable interfacial magnetic anisotropy in the Pt/Ni bilayer, which differs significantly from that of the Pt/Py bilayer, with a near-zero magnetostrictive coefficient and a high

Curie temperature. These distinct magnetic properties of the Pt/Ni/Py trilayer may lead to the expected dynamical properties that differ from the previously observed spin dynamics in the Pt/Py-based SHNO. The evolutionary behavior of the characteristics of the oscillation spectra on the excitation current of the SHNO is generally used as an essential indicator to analyze the nature of the dynamical states. Therefore, we first investigate the dependence of the spectral characteristics on the excitation current I at different magnetic fields with several polar angles.

Figure 4 shows pseudocolor maps of the representative current dependence of the microwave power spectral density (PSD) generated by our device at various polar angles φ. A single mode with the central frequency slightly below the FMR frequency f_{FMR} (represented by the dashed lines) of the Pt/Ni/Py trilayer film is observed above the critical current I_c, the low polar angles $\varphi \leq 50°$, and the low field $H = 1000$ Oe [Figs. 4(a)–4(d)]. We note that the Oersted field of the current in Pt-based SHNOs opposes the in-plane component of an external field, reducing the frequency of the auto-oscillation [36]. The oscillation peak frequency stays near constant with increasing current I until its intensity increases to its maximum at around $I = 25$ mA and it then turns into a sharp red shift accompanying the peak broadening with increasing current. The more significant frequency red shift than the
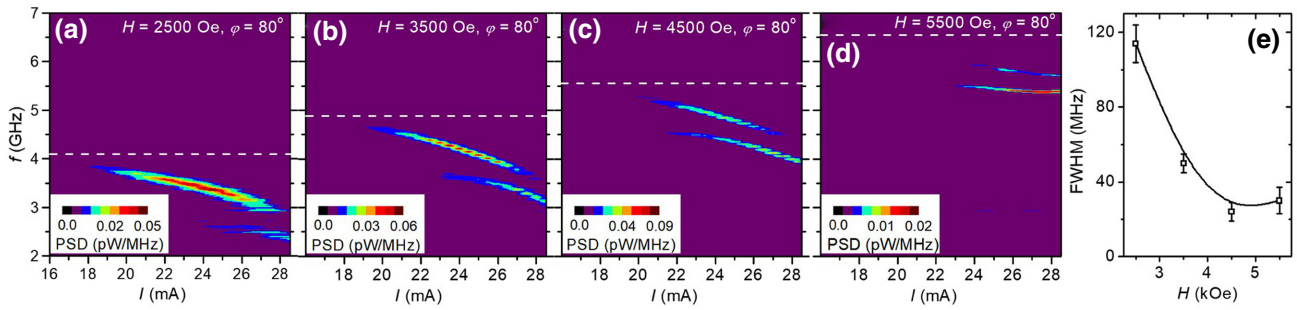
FIG. 5. The dependence of the microwave-generation characteristics of the SHNO on the current. (a)–(d) Pseudocolor maps of the current-dependent spectra obtained at $T = 6$ K, oblique angle $\varphi = 80°$, and four different magnetic fields: (a) $H = 2500$ Oe, (b) 3500 Oe, (c) 4500 Oe, and (d) 5500 Oe. The dashed curves represent the corresponding FMR frequencies, f_{FMR}, of the Pt/Ni/Py trilayer. (e) The dependence of the minimum line width of the first high-frequency mode on the tilt magnetic fields. The solid curve is given as a guide to the eye.

previously reported Py/Pt-based SHNO indicates that the Pt/Ni/Py-based SHNO has a more significant nonlinear coefficient, which may be related to its large magnetostriction and interfacial magnetic anisotropy. Furthermore, when the magnitude and tilt angle of the applied external magnetic field increases to $H \geq 2000$ Oe and $\varphi \geq 55°$, the magnetization of the Pt/Ni/Py trilayer will deviate from the film plane and form a sizable oblique angle by following the external field. Under $H \geq 2000$ Oe and $\varphi \geq 55°$, except for the high-frequency peak, another peak with a lower frequency is also observed [Figs. 4(e)–4(h)].

To further explore the relationship between the observed two dynamical modes and the field and/or current, we examine the current dependence of the generation spectrum at several external fields H with a constant polar angle, $\varphi = 80°$ (Fig. 5). The dashed line shows the FMR frequency, f_{FMR}, determined by ST FMR. These data indicate that the first and second modes both have a similar and strong red shift with increasing current and that their frequencies remain far below f_{FMR} in all of the studied fields. On the basis of this behavior and the

results of previous microwave spectra [6,36], microfocus Brillouin light scattering [5], and micromagnetic simulations of nano-oscillators [36,51], the two modes belong to a nonpropagating self-localized "bullet" spin wave [52]. The current dependence of the oscillating peaks for different fields suggests that the first mode is suppressed by increasing the out-of-plane field, while the second low-frequency mode is facilitated. In addition, the line width of the first mode decreases sharply to approximately 25 MHz at 4.5 kOe from approximately 115 MHz at 2.5 kOe and then maintains a weak change with a further increasing field, which suggests that the broad line width is mainly caused by the large magnetostriction and MA-induced inhomogeneous magnetization at low field. The nonlinear-coefficient-induced frequency red shift at $H = 5.5$ kOe also becomes much weaker than that at the low fields.

To get the detailed evolution of the two self-localized modes with the out-of-plane field, we analyze the dependence of the generation spectra on the field with oblique angle $\varphi = 80°$ for several applied currents I (Fig. 6). At a low current, $I = 19$ mA, the first high-frequency mode is
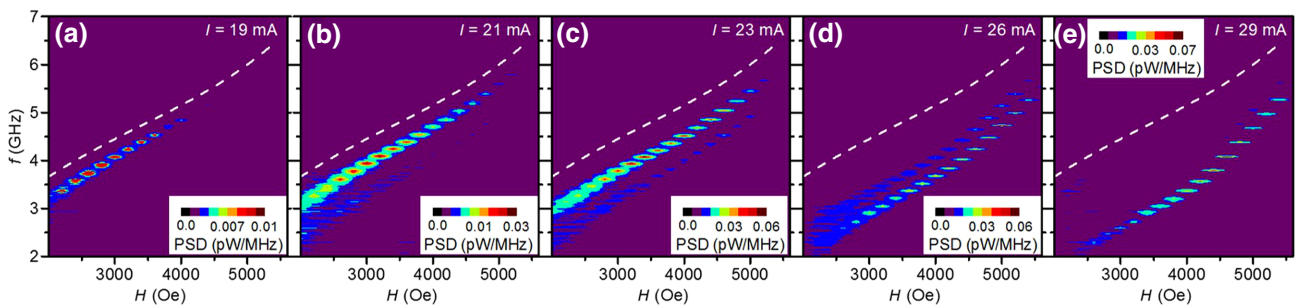

FIG. 6. The dependence of the microwave-generation characteristics of the SHNO on the oblique magnetic field. (a)–(e) Pseudocolor plots of the field-dependent spectra with $H = 200$ Oe steps obtained at 6 K, $\varphi = 80°$, and five different excited currents (a) $I = 19$ mA, (b) $I = 21$ mA, (c) $I = 23$ mA, (d) $I = 26$ mA, and (e) $I = 29$ mA. The dashed curve represents the experimental f_{FMR} versus H dispersion curve of the Pt/Ni/Py trilayer.
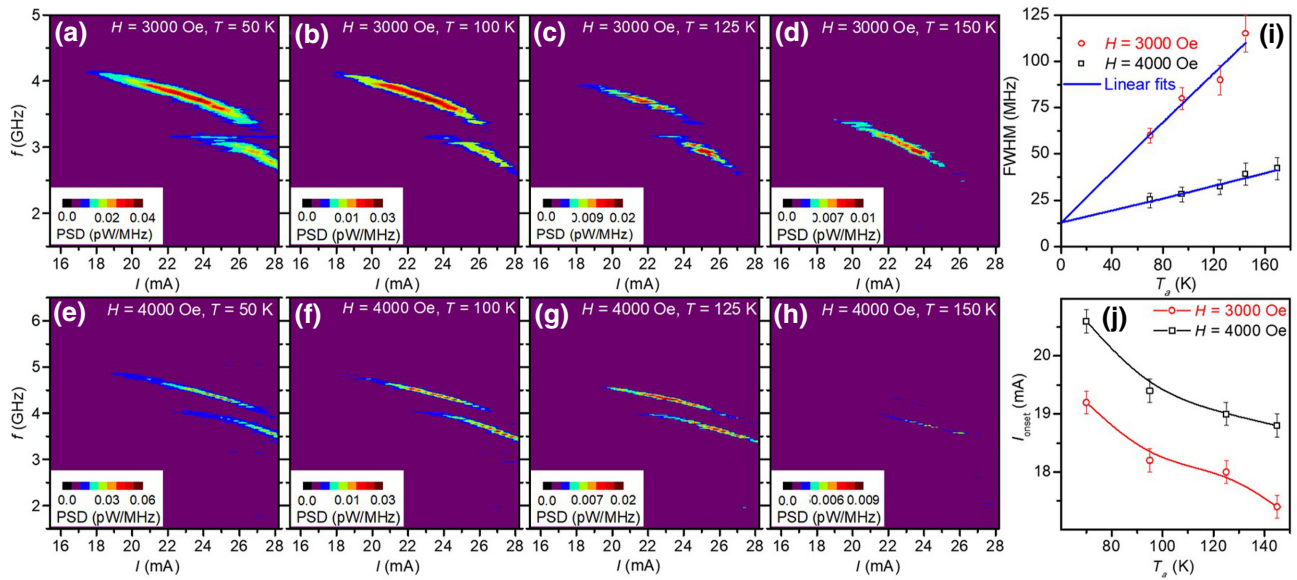
FIG. 7. The dependence of the microwave-generation characteristics on the current at different temperatures T, $\varphi = 80°$, and two different fields, $H = 3000$ Oe and $H = 4000$ Oe. (a)–(d) Pseudocolor plots of the current-dependent spectra obtained at $H = 3000$ Oe, above I_c increased in 0.4-mA steps, at (a) $T = 50$ K, (b) $T = 100$ K, (c) $T = 125$ K, and (d) $T = 150$ K. (e)–(h) The same as (a)–(d) except for $H = 4000$ Oe. (i) The actual temperature T_a versus the minimum line width, defined by the full width at half maximum (FWHM), corresponding to the highest-intensity peak of the PSD spectra, determined by fitting the spectra of (a)–(h) with a Lorentzian function. The solid lines are the linear fits. (j) The dependence of the onset current I_{onset} on the actual temperature T_a of the active device regime, determined by comparing current-dependent resistance data at different temperatures T and the temperature-dependent resistance of the device measured at a small current of $I = 0.1$ mA. The solid curves are given as guides to the eye.

only excited for the range $H \le 4$ kOe and its oscillating frequency is slightly lower than f_{FMR}, which is represented as the dashed line [Fig. 6(a)]. When the applied current I increases to 21 mA, the intensity of the first oscillating mode continues to be enhanced, with the accompaning appearance of another low-frequency peak, and the oscillation field region of the first mode also extends to near 5.5 kOe, which suggests that the higher excitation current is required to generate a spin wave at larger fields. With further increase of the current, the frequencies of both modes continue to drop due to the above-mentioned negative nonlinear-coefficient-induced strong frequency red shift, especially for the low-field range $H \le 4.5$ kOe. Above 29 mA, the first oscillating peak vanishes and only the second oscillating peak with a central frequency far below f_{FMR} is observed in the microwave-generation spectra [Fig. 6(e)].

D. Temperature effect of current-driven dynamical modes

To gain further insight into the thermal effects on the characteristics of the two localized modes, we carry out spectroscopic measurements with two selected oblique fields, $H = 3$ kOe and $H = 4$ kOe, at different cryogenic temperatures from 6 K to 150 K. Figure 7 shows the

dependence of the spectral characteristics on I with a polar angle of $\varphi = 80°$ at different temperatures. Like the representative spectra obtained at 6 K in Fig. 5, the current-dependent spectra observed at high temperature exhibit similar overall behavior. The high-frequency mode is first observed at a small current, it coexists with another low-frequency mode at the intermediate-current range, and finally it disappears with only the low-frequency mode at the large currents surviving. Figures 7(d) and 7(h) show that the high-frequency mode is completely destroyed by the thermal fluctuation at 150 K.

There is no detectable oscillation peak observed in the microwave-generation spectrum at $T > 150$ K, which is much lower than the critical temperature in previously reported Py/Pt-based nanogap SHNOs, which is likely associated with two factors: that there is a much lower Curie temperature for the thin nickel film than for Py and that there is a higher driving-current-induced more significant Joule heating in the active device area due to its large magnetic damping constant $\alpha \sim 0.047$, compared to 0.028 in the Pt/Py bilayer. We can estimate the actual device-area temperature T_a by taking into account current-induced Joule heating via directly comparing the R versus I and R versus T curves of the studied device [6]. Figure 7(j) shows that the onset current I_{onset} of the first high-frequency mode exhibits a substantial decrease with increasing T_a, consistent with several previously reported

Pt-based spin-torque nano-oscillators [6,40]. According to the previous studies [6,18–20,53], the observed reduction in the driving current with increasing T_a is likely related to an increase of the bulk spin Hall effect in Pt, the interfacial Rashba-effect-induced SOT efficiency in the ultrathin Pt-FM system, and a decrease of the magnetic damping of the thin magnetic Ni/Py layer due to the decline of the interfacial MA with increasing temperature. Additionally, the relative independent-temperature oscillation frequency indicates that the weak temperature-dependent saturation magnetization M_s does not seem to be the reason for a substantial decrease in I_{onset}.

The temperature dependence of the oscillation line width provides further information about the thermal effect on the spin-current-driving magnetization oscillation coherence. To avoid the possible contribution due to the current-dependent variation of nonlinearity, we choose the minimum line width of the first localized mode to analyze its temperature dependence, as shown in Fig. 7(i). The minimum line width shows a linear dependence on temperature T_a, as illustrated for two large oblique fields, $H = 3$ kOe and $H = 4$ kOe. This linear behavior proportional to temperature is as predicted by the nonlinear theory of thermal broadening and the thermal-noise model for spin-torque nano-oscillators (STNOs) [54,55] and is also consistent with the previously reported vertical nanocontact spin Hall nano-oscillator under large oblique fields [40], traditional spin-transfer-torque nano-oscillators [56,57], and magnetic vortex nano-oscillators [58].

However, the linear dependence is contrasted with the thermal effects in planar-nanogap Py/Pt-based SHNOs with a negligible magnetic anisotropy under in-plane field geometry, where the line width increases exponentially with the temperature due to thermally activated transitions between different dynamical modes [6]. The Pt/Ni/Py trilayer has a large interface-induced magnetic anisotropy with $H_k = 1.82$ kOe, determined by the f_{FMR} versus H_{res} and φ versus H_{res} dispersion relations obtained by ST FMR above, the strong lateral anisotropy variation, and the magnetoelastic coefficient, which are supported by the large magnetic inhomogeneous FMR line-width broadening $\Delta H_0 = 28$ Oe and the magnetic damping constant $\alpha = 0.047$. These variations can cause sizable variations of the internal magnetic field on the active device area and consequently result in the self-localized spin-wave modes, with different frequencies separately localized in different regions. Meanwhile, the potential barrier between the two spin-oscillation regimes can effectively suppress the thermally activated transition among the different modes observed in planar-nanogap Py/Pt-based SHNOs [6]. The large interception value of 12.5 MHz at zero temperature, determined by the linear fit to the line width results obtained at $H = 3$ kOe and $H = 4$ kOe, also supports the above argument.

IV. CONCLUSIONS

To summarize, we quantitatively calculate the effective SOT efficiency arising from the bulk SHE of Pt and the interfacial Rashba effect in a Pt/Ni/Py trilayer structure by using the ST-FMR technique and find that its effective dampinglike torque efficiency $\xi_{DL} \sim 0.055$ and that there is a non-negligible fieldlike torque with opposite sign compared with the previously reported Pt/Py, Pt/Co, and Pt/Fe bilayer systems. In addition, we systematically investigate the exciting current and magnitude, the angle of the applied magnetic field, and the temperature dependence of the microwave-generation spectral characteristics of an SHNO with a Pt/Ni/Py trilayer. At low oblique angles $\varphi \leq 50°$, the microwave-generation spectra exhibit a single Lorentzian peak with the center frequency below f_{FMR} and a significant frequency red shift with an increase in the applied current, which strongly resembles the spectral characteristics of the nonlinear self-localized bullet mode identified in the similar planar-nanogap SHNOs with a Pt/Py bilayer.

In contrast, at high oblique angles $\varphi \geq 55°$, the spectra show two distinct oscillating peaks with very similar field-, current- and temperature-dependent behavior, which suggests that they belong to the same type of bullet mode and maintain spatial coexistence at certain currents and magnetic fields. Unlike the previously observed exponential temperature dependence of the line width related to thermally activated transitions between different dynamical modes in Pt/Py-based SHNOs with negligible magnetic anisotropy and magnetostriction, a linear temperature dependence of the minimum line width, which resembles the thermal broadening of single-mode oscillation, is observed in Pt/Ni/Py-based SHNOs. This indicates that the decoherence of the SOT-driven oscillating dynamic mode arising from thermally activated mode transitions can be avoided by creating an appreciable potential barrier between two spatially separated local bullet modes via spatially varied magnetic anisotropy, magnetostriction, or magnetic defects at the Pt-Ni and Ni-Py interfaces. The results of the SOT efficiency and SOT-driven magnetic dynamics in SHNOs with a Pt/Ni/Py trilayer can extend the development of spin-orbitronic materials.

[1] I. M. Miron, G. Gaudin, S. Auffret, B. Rodmacq, A. Schuhl, S. Pizzini, J. Vogel, and P. Gambardella, Current-Driven Spin Torque Induced by the Rashba Effect in a Ferromagnetic Metal Layer, Nat. Mater. **9**, 230 (2010).

[2] L. Liu, O. J. Lee, T. J. Gudmundsen, D. C. Ralph, and R. A. Buhrman, Current-Induced Switching of Perpendicularly Magnetized Magnetic Layers Using Spin Torque from the Spin Hall Effect, Phys. Rev. Lett. **109**, 096602 (2012).

[3] L. Liu, C.-F. Pai, Y. Li, H. Tseng, D. Ralph, and R. Buhrman, Spin-torque switching with the giant spin Hall effect of tantalum, Science **336**, 555 (2012).

[4] G. Yu, P. Upadhyaya, Y. Fan, J. G. Alzate, W. Jiang, K. L. Wong, S. Takei, S. A. Bender, L.-T. Chang, Y. Jiang, M. Lang, J. Tang, Y. Wang, Y. Tserkovnyak, P. K. Amiri, and K. L. Wang, Switching of perpendicular magnetization by spin-orbit torques in the absence of external magnetic fields, Nat. Nanotechnol. **9**, 548 (2014).

[5] V. E. Demidov, S. Urazhdin, H. Ulrichs, V. Tiberkevich, A. Slavin, D. Baither, G. Schmitz, and S. O. Demokritov, Magnetic nano-oscillator driven by pure spin current, Nat. Mater. **11**, 1028 (2012).

[6] R. H. Liu, W. L. Lim, and S. Urazhdin, Spectral Characteristics of the Microwave Emission by the Spin Hall Nano-Oscillator, Phys. Rev. Lett. **110**, 147601 (2013).

[7] A. Brataas, A. D. Kent, and H. Ohno, Current-induced torques in magnetic materials, Nat. Mater. **11**, 372 (2012).

[8] A. Manchon, J. Zelezny, I. M. Miron, T. Jungwirth, J. Sinova, A. Thiaville, K. Garello, and P. Gambardella, Current-induced spin-orbit torques in ferromagnetic and antiferromagnetic systems, Rev. Mod. Phys. **91**, 035004 (2019).

[9] Y. Cao, G. Xing, H. Lin, N. Zhang, H. Zheng, and K. Wang, Prospect of Spin-Orbitronic Devices and Their Applications, iScience **10**, 101614 (2020).

[10] M. Zahedinejad, A. A. Awad, S. Muralidhar, R. Khymyn, H. Fulara, H. Mazraati, M. Dvornik, and J. Åkerman, Two-dimensional mutually synchronized spin Hall nano-oscillator arrays for neuromorphic computing, Nat. Nanotechn. **15**, 47 (2020).

[11] L. Li, L. Chen, R. Liu, and Y. Du, Recent progress on excitation and manipulation of spin-waves in spin Hall nano-oscillators, Chin. Phys. B **29**, 117102 (2020).

[12] B. Dieny, I. L. Prejbeanu, and K. Garello *et al.*, Opportunities and challenges for spintronics in the microelectronics industry, Nat. Electron. **3**, 446 (2020).

[13] J. E. Hirsch, Spin Hall Effect, Phys. Rev. Lett. **83**, 1834 (1999).

[14] A. Hoffmann, Spin Hall effects in metals, IEEE Trans. Magn. **49**, 5172 (2013).

[15] J. Sinova, S. O. Valenzuela, J. Wunderlich, C. H. Back, and T. Jungwirth, Spin Hall effects, Rev. Mod. Phys. **87**, 1213 (2015).

[16] V. P. Amin and M. D. Stiles, Spin transport at interfaces with spin-orbit coupling: Phenomenology, Phys. Rev. B **94**, 104420 (2016).

[17] V. P. Amin, P. M. Haney, and M. D. Stiles, Interfacial spin-orbit torques, J. Appl. Phys. **128**, 151101 (2020).

[18] C.-F. Pai, Y. Ou, L. H. Vilela-Leao, D. C. Ralph, and R. A. Buhrman, Dependence of the efficiency of spin Hall torque on the transparency of Pt/ferromagnetic layer interfaces, Phys. Rev. B **92**, 064426 (2015).

[19] L. J. Zhu, D. C. Ralph, and R. A. Buhrman, Spin-Orbit Torques in Heavy-Metal–Ferromagnet Bilayers with Varying Strengths of Interfacial Spin-Orbit Coupling, Phys. Rev. Lett. **122**, 077201 (2019).

[20] K. Gupta, R. J. H. Wesselink, R. X. Liu, Z. Yuan, and P. J. Kelly, Disorder Dependence of Interface Spin Memory Loss, Phys. Rev. Lett. **124**, 087702 (2020).

[21] G. Dresselhaus, Spin-Orbit Coupling Effects in Zinc Blende Structures, Phys. Rev. **100**, 580 (1955).

[22] Y. A. Bychkov and E. I. Rashba, Oscillatory effects and the magnetic susceptibility of carriers in inversion layers, J. Phys. C **17**, 6039 (1984).

[23] R. H. Liu, W. L. Lim, and S. Urazhdin, Control of current-induced spin-orbit effects in a ferromagnetic heterostructure by electric field, Phys. Rev. B **89**, 220409(R) (2014).

[24] T. Wang, W. Wang, Y. Xie, M. A. Warsi, J. Wu, Y. Chen, V. O. Lorenz, X. Fan, and J. Q. Xiao, Large spin Hall angle in vanadium film, Sci. Rep. **7**, 1306 (2017).

[25] Q. Guo, Z. Ren, H. Bai, X. Wang, G. Yu, W. He, J. Teng, and T. Zhu, Current-induced magnetization switching in perpendicularly magnetized V/CoFeB/MgO multilayers, Phys. Rev. B **104**, 224429 (2021).

[26] L. Ni, Z. Chen, X. Lu, Y. Yan, L. Jin, J. Zhou, W. Yue, Z. Zhang, L. Zhang, and W. Wang *et al.*, Strong interface-induced spin-charge conversion in YIG/Cr heterostructures, Appl. Phys. Lett. **117**, 112402 (2020).

[27] R. H. Liu, L. Chen, S. Urazhdin, and Y. W. Du, Controlling the Spectral Characteristics of a Spin-Current Auto-Oscillator with an Electric Field, Phys. Rev. Appl. **8**, 021001(R) (2017).

[28] M. Ranjbar, P. Drrenfeld, M. Haidar, E. Iacocca, M. Balinskiy, T. Q. Le, M. Fazlali, A. Houshang, A. Awad, R. K. Dumas, and J. Åkerman, CoFeB-based spin Hall nano-oscillators, IEEE Magn. Lett. **5**, 3000504 (2014).

[29] V. E. Demidov, S. Urazhdin, A. Zholud, A. V. Sadovnikov, and S. O. Demokritov, Nanoconstriction-based spin-Hall nano-oscillator, Appl. Phys. Lett. **105**, 172410 (2014).

[30] Z. Duan, A. Smith, L. Yang, B. Youngblood, J. Lindner, V. E. Demidov, S. O. Demokritov, and I. N. Krivorotov, Nanowire spin torque oscillator driven by spin orbit torques, Nat. Commun. **5**, 1038 (2014).

[31] R. H. Liu, W. L. Lim, and S. Urazhdin, Dynamical Skyrmion State in a Spin Current Nano-Oscillator with Perpendicular Magnetic Anisotropy, Phys. Rev. Lett. **114**, 137201 (2015).

[32] H. Mazraati, S. Chung, A. Houshang, M. Dvornik, L. Piazza, F. Qejvanaj, S. Jiang, T. Q. Le, J. Weissenrieder, and J. Åkerman, Low operational current spin Hall nano-oscillators based on NiFe/W bilayers, Appl. Phys. Lett. **109**, 242402 (2016).

[33] M. Collet, X. de Milly, O. d'Allivy Kelly, V. V. Naletov, R. Bernard, P. Bortolotti, J. Ben Youssef, V. E. Demidov, S. O. Demokritov, J. L. Prieto, M. Munoz, V. Cros, A. Anane, G. de Loubens, and O. Klein, Generation of coherent spin-wave modes in yttrium iron garnet microdiscs by spin-orbit torque, Nat. Commun. **7**, 10377 (2016).

[34] M. B. Jungfleisch, W. Zhang, J. Sklenar, J. Ding, W. Jiang, H. Chang, F. Y. Fradin, J. E. Pearson, J. B. Ketterson, V.

Novosad, M. Wu, and A. Hoffmann, Large Spin-Wave Bullet in a Ferrimagnetic Insulator Driven by the Spin Hall Effect, Phys. Rev. Lett. **116**, 057601 (2016).

[35] H. Fulara, M. Zahedinejad, R. Khymyn, A. A. Awad, S. Muralidhar, M. Dvornik, and J. Akerman, Spin-orbit torque-driven propagating spin waves, Sci. Adv. **5**, 9 (2019).

[36] L. Chen, K. Zhou, S. Urazhdin, W. Jiang, Y. W. Du, and R. H. Liu, Dynamical mode coexistence and chaos in a nanogap spin Hall nano-oscillator, Phys. Rev. B **100**, 104436 (2019).

[37] A. A. Awad, P. Drrenfeld, A. Houshang, M. Dvornik, E. Iacocca, R. K. Dumas, and J. Åkerman, Long-range mutual synchronization of spin Hall nano-oscillators, Nat. Phys. **13**, 292 (2017).

[38] L. Chen, S. Urazhdin, Y. W. Du, and R. H. Liu, Dynamical Mode Coupling and Coherence in a Spin Hall Nano-Oscillator with Perpendicular Magnetic Anisotropy, Phys. Rev. Appl. **11**, 064038 (2019).

[39] H. Fulara, M. Zahedinejad, R. Khymyn, M. Dvornik, S. Fukami, S. Kanai, H. Ohno, and J. Åkerman, Giant voltage-controlled modulation of spin Hall nano-oscillator damping, Nat. Commun. **11**, 1 (2020).

[40] L. Chen, S. Urazhdin, K. Zhou, Y. W. Du, and R. H. Liu, Magnetic Droplet Mode in a Vertical Nanocontact-Based Spin Hall Nano-Oscillator at Oblique Fields, Phys. Rev. Appl. **13**, 024034 (2020).

[41] D. Backes, F. Maci, S. Bonetti, R. Kukreja, H. Ohldag, and A. D. Kent, Direct Observation of a Localized Magnetic Soliton in a Spin-Transfer Nanocontact, Phys. Rev. Lett. **115**, 127205 (2015).

[42] D. Go, F. Freimuth, J. P. Hanke, F. Xue, O. Gomonay, K. J. Lee, S. Blugel, P. M. Haney, H. W. Lee, and Y. Mokrousov, Theory of current-induced angular momentum transfer dynamics in spin-orbit coupled systems, Phys. Rev. Res. **2**, 033401 (2020).

[43] H. Hayashi, A. Musha, H. Sakimura, and K. Ando, Spin-orbit torques originating from the bulk and interface in Pt-based structures, Phys. Rev. Res. **3**, 013042 (2021).

[44] L. Liu, T. Moriyama, D. C. Ralph, and R. A. Buhrman, Spin-Torque Ferromagnetic Resonance Induced by the Spin Hall Effect, Phys. Rev. Lett. **106**, 036601 (2011).

[45] L. Yang, Y. Fei, K. Zhou, L. Chen, Q. Fu, L. Li, C. Yan, H. Li, Y. W. Du, and R. H. Liu, Maximizing spin-orbit torque efficiency of Ta(O)/Py via modulating oxygen-induced interface orbital hybridization, Appl. Phys. Lett. **118**, 032405 (2021).

[46] T. R. Mcguier and R. I. Potter, Anisotropic magnetoresistance in ferromagnetic 3*d* alloys, IEEE Trans. Mag. **4**, 1018 (1975).

[47] S. Zhang, P. M. Levy, and A. Fert, Mechanisms of Spin Polarized Current-Driven Magnetization Switching, Phys. Rev. Lett. **88**, 236601 (2002).

[48] S. Petit, C. Baraduc, C. Thirion, U. Ebels, Y. Liu, M. Li, P. Wang, and B. Dieny, Spin-Torque Influence on the High Frequency Magnetization Fluctuations in Magnetic Tunnel Junctions, Phys. Rev. Lett. **98**, 077203 (2007).

[49] S. Mizukami, Y. Ando, and T. Miyazaki, The study on ferromagnetic resonance linewidth for NM/^{80}NiFe/NM (NM = Cu, Ta, Pd and Pt) films, Jpn. J. Appl. Phys. **40**, 580 (2001).

[50] L. Ni, Z. Chen, W. Li, X. Lu, Y. Yan, L. Zhang, C. Yan, Y. Chen, Y. Gu, and Y. Li *et al.*, Magnetic dynamics of two-dimensional itinerant ferromagnet Fe$_3$GeTe$_2$, Chin. Phys. B **9**, 097501 (2021).

[51] H. Ulrichs, V. E. Demidov, and S. O. Demokritov, Micromagnetic study of auto-oscillation modes in spin-Hall nano-oscillators, Appl. Phys. Lett. **104**, 042407 (2014).

[52] A. Slavin and V. Tiberkevich, Spin Wave Mode Excited by Spin-Polarized Current in a Magnetic Nanocontact is a Standing Self-Localized Wave Bullet, Phys. Rev. Lett. **95**, 237201 (2005).

[53] S. Lendínez, J. Hang, S. Vélez, J. M. Hernández, D. Backes, A. D. Kent, and F. Macià, Effect of Temperature on Magnetic Solitons Induced by Spin-Transfer Torque, Phys. Rev. Appl. **7**, 054027 (2017).

[54] V. S. Tiberkevich, A. N. Slavin, and J. V. Kim, Temperature dependence of nonlinear auto-oscillator linewidths: Application to spin-torque nano-oscillators, Phys. Rev. B **78**, 092401 (2008).

[55] T. J. Silva and M. W. Keller, Theory of Thermally Induced Phase Noise in Spin Torque Oscillators for a High-Symmetry Case, IEEE Trans. Magn. **46**, 3555 (2010).

[56] M. L. Schneider, W. H. Rippard, M. R. Pufall, T. Cecil, T. J. Silva, and S. E. Russek, Temperature dependence of spin-torque-driven self-oscillations, Phys. Rev. B **80**, 144412 (2009).

[57] J. F. Sierra, M. Quinsat, F. Garcia-Sanchez, U. Ebels, I. Joumard, A. S. Jenkins, B. Dieny, M. C. Cyrille, A. Zeltser, and J. A. Katine, Influence of thermal fluctuations on the emission linewidth in MgO-based spin transfer oscillators, Appl. Phys. Lett. **101**, 062407 (2012).

[58] P. Bortolotti, A. Dussaux, J. Grollier, V. Cros, A. Fukushima, H. Kubota, K. Yakushiji, S. Yuasa, K. Ando, and A. Fert, Temperature dependence of microwave voltage emission associated to spin-transfer induced vortex oscillation in magnetic tunnel junction, Appl. Phys. Lett. **100**, 042408 (2012).